Carbonation of Hydrous Materials at the Molecular Level: a ToF-SIMS, Raman and DFT study

Giovanni L. Pesce[1], Ian Fletcher[2], James Grant[3], Marco Molinari[3], Stephen C. Parker[3,], Richard J. Ball[1]*

[1] University of Bath, Department of Arch. and Civil Engineering, Bath, BA2 7AY, UK

[2] Intertek Wilton Laboratory, The Wilton Centre, Redcar, TS10 4RF, UK

[3] University of Bath, Department of Chemistry, Bath, BA2 7AY, UK

Carbonation of hydrous minerals such as calcium hydroxide ($Ca(OH)_2$), is an important process in environmental and industrial applications for the construction industry, geological disposal repositories for nuclear waste, and green technologies for carbon capture. Although the role of ions during the carbonation mechanism of $Ca(OH)_2$ is still unclear, we identified the exchange of ions during the dissolution-and-precipitation process, by determining the change in isotopic composition of carbonation products using Time-of-Flight Secondary Ion Mass Spectrometry. Our samples of pure $Ca(^{18}OH)_2$ carbonated in air were characterized using Scanning Electron Microscopy and Raman spectroscopy, aided by Density Functional Theory calculations. Our results show that the carbonation process at high pH is a two-stage mechanism. The first stage occurs in a short time after $Ca(^{18}OH)_2$ is exposed to air and involved the dissolution of surface Ca ions and hydroxyl ^{18}OH groups, which reacts directly with dissolved CO_2, leading to 1/3 of ^{18}O in the oxygen content of carbonate phases. The second stage occurs within 24h of exposure allowing a rebalance of the oxygen isotopic composition of the carbonate phases with higher content of ^{16}O.

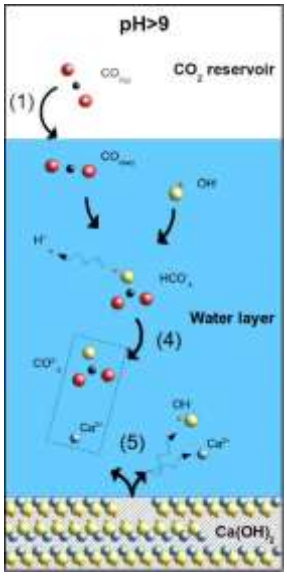

Prof. Steve Parker
Department of Chemistry
University of Bath
BA2 7AY, Bath
United Kingdom,
E: S.C.Parker@bath.ac.uk
P: +44 (0)1225 386505

Carbonation of Hydrous Materials at the Molecular Level: a ToF-SIMS, Raman and DFT study

Giovanni L. Pesce[1, i], Ian Fletcher[2, ii], James Grant[3], Marco Molinari[3], Stephen C. Parker[3,], Richard J. Ball[1]*

[1] University of Bath, Department of Arch. and Civil Engineering, Bath, BA2 7AY, UK

[2] Intertek Wilton Laboratory, The Wilton Centre, Redcar, TS10 4RF, UK

[3] University of Bath, Department of Chemistry, Bath, BA2 7AY, UK

* Corresponding authors: Stephen C. Parker, S.C.Parker@bath.ac.uk, phone: +44 (0)1225 386505

[i] Currently at Northumbria University, Department of Architecture and Built Environment, Newcastle upon Tyne, NE1 8ST, UK

[ii] Currently at Newcastle University, School of Mechanical and Systems Engineering, Newcastle upon Tyne, NE1 7RU, UK

Abstract

Carbonation of hydrous minerals such as calcium hydroxide ($Ca(OH)_2$), is an important process in environmental and industrial applications for the construction industry, geological disposal repositories for nuclear waste and green technologies for carbon capture. Although the role of ions during the carbonation mechanism of $Ca(OH)_2$ is still unclear, we identified the exchange of ions during the dissolution-and-precipitation process, by determining the change in isotopic composition of carbonation products using Time-of-Flight Secondary Ion Mass Spectrometry. Our samples of pure $Ca(^{18}OH)_2$ carbonated in air were characterized using Scanning Electron Microscopy and Raman spectroscopy, aided by Density Functional Theory calculations.

Our results show that the carbonation process at high pH is a two-stage mechanism. The first stage occurs in a short time after $Ca(^{18}OH)_2$ is exposed to air and involved the dissolution of surface Ca ions and hydroxyl ^{18}OH groups, which reacts directly with dissolved CO_2, leading to 1/3 of ^{18}O in the oxygen content of carbonate phases. The second stage occurs within 24h of exposure allowing a rebalance of the oxygen isotopic composition of the carbonate phases with higher content of ^{16}O.

Introduction

The carbonation process of hydrous materials and minerals such as calcium and magnesium hydroxides ($Ca(OH)_2$ and $Mg(OH)_2$, respectively) is important for a number of environmental and technological applications. These include carbon capture and storage (CCS)[1,2], scrubbing procedures of solid waste incinerators[3], emerging low carbon building technologies for construction[4-6], and geological disposal repositories for nuclear waste[7,8] where portlandite content in cements becomes a critical factor. Despite its importance,[2,4,9-14] the carbonation mechanism in high pH environments is debated and not yet fully understood. Hence, to devise successful and efficient strategies for carbon dioxide (CO_2) sequestration, soil stabilization in geoengineering and building mortars with enhanced properties, a clear understanding of the details of carbonation mechanisms is required.

Two carbonation mechanisms have been proposed for portlandite at standard conditions, 25°C and 1atm, based on solid state and a dissolution-carbonation[15-19] processes (the former is highly unlikely whereas the latter has been documented in a number of cases). Moorehead[20] suggested that carbonation of $Ca(OH)_2$ at room temperature in CO_2-rich environments is a solid-state reaction, which entails substitution of hydroxyl groups (OH^-) with carbonate groups (CO_3^{2-}) in a topotactic transition, leading to a change of the portlandite $d_{\{001\}}$ spacing.[11,20-22] Other authors suggested that the reaction occurs via a dissolution-and-precipitation mechanism catalyzed by water molecules adsorbed on the mineral surfaces[11,23,26] Overall, these two mechanisms would be expected to lead to different reaction rates, and result in the formation of passivating carbonate layers[25] effectively quenching the exploitation of $Ca(OH)_2$ surface properties.[11]

Recent work by Rodriguez-Navarro and colleagues has involved detailed analysis of calcium carbonate formation from saturated solution and through the carbonation of calcium hydroxide nano-particles.[26-27] These show that the formation of thermodynamically stable calcite can proceed through a cascade of hydrated and dehydrated amorphous calcium carbonate phases and include (or not) intermediate crystalline phases of vaterite and/or aragonite. In addition to the requirement for CO_2 for carbonation the presence of water, adsorbed from a high RH atmosphere was demonstrated. In the first instance the aim of the present work is to show that artificial doping of isotopes can be used to trace the history of the species involved in the formation of carbonate ions, and thus shed light on the mechanisms of portlandite carbonation.

The natural variation of stable isotopes, such as carbon-13 (^{13}C) or oxygen-18 (^{18}O), can be exploited in the study of carbonation of surfaces, and thus provide complementary results to other techniques.[29-32] An isotope can be traced during chemical reactions and, as different reaction mechanisms lead to different products with distinctive isotopic compositions[29-34], it provides insights on the stages occurring during the reaction. Our research investigated the role of OH^- ions in the carbonation mechanism of $Ca(OH)_2$ by using Time-of-Flight Secondary Ion Mass Spectrometry (ToF-SIMS) on an artificial $Ca(^{18}OH)_2$ sample carbonated in air (rich in ^{16}O) for 3 minutes (at 27% RH), 1, 8

and 137 days (50% RH). Samples were characterized using Scanning Electron Microscopy (SEM) and Raman spectroscopy. Density functional theory calculations were also employed to corroborate the Raman shifts associated with different degrees of isotopic substitution in $Ca(OH)_2$ and $CaCO_3$. We finally discuss critical factors in the carbonation process, which provides new insights of the carbonation mechanism of $Ca(OH)_2$.

Experimental and Theoretical Methods

Material preparation

^{18}O-calcium hydroxide was produced by reacting calcium metal of 99% purity with isotopic labelled water containing >99% ^{18}O (Taiyo Nippon Sanso Corporation), on a platinum (Pt) foil 99.9% pure. To prevent oxygen contamination and carbonation of the $Ca(OH)_2$ sample, the reaction was performed in an inert atmosphere inside a glove bag filled with nitrogen, where CO_2 and RH were monitored using a K-30 10,000ppm sensor for CO_2, and a DHT22 sensor for temperature and humidity. Both sensors were controlled via an Arduino Uno microcontroller, which was also used for real time monitoring of the conditions.

Experiments were conducted as follows. 1) The equipment and materials were placed into a glove bag that was then filled with nitrogen. 2) The residual air in the bag was flushed using dry nitrogen until the sensor readings were 0 ppm CO_2 and <5% RH. 3) 20mg of Ca metal was weighed on a precision balance and deposited on a Pt foil, positioned inside an open crucible. 4) 800µl of ^{18}O-water was reacted with the Ca metal using a glass Hamilton syringe equipped with a metal needle. The reaction was carried out in an excess of ^{18}O-water to promote the complete reaction of Ca. 5). To ensure the complete evaporation of excess of ^{18}O-water, the bag was flushed several times with dry nitrogen. 6) When the majority of the water had evaporated, portions of the sample were removed from the Pt foil. Portions were sealed inside a glass cell with a quartz window for the Raman analysis; the N_2-rich atmosphere prevented carbonation before completion of the analysis. The same procedure was followed for samples for SEM analysis except samples were placed in a

small vial and stored under low vacuum. Material for SIMS analysis remained on the Pt foil and stored in a glass vial under low vacuum.

ToF-SIMS analysis

In order to study the isotopic composition of carbonates at the very beginning of the reaction, the first ToF-SIMS analysis was carried out after approximately 3 minutes exposure to air at 23˚±2°C and 27±10% RH. Low RH levels were maintained to minimize the carbonation rate.[26] After initial analysis, the samples were removed from the instrument and allowed to stand in a dust-free controlled environment at 23±2°C and 50±10% RH for 1, 8 and 138 days before further analysis. Care was taken to analyze fresh areas of the samples that had not previously been exposed to the ion and electron beams. An Analar $CaCO_3$ powder was analyzed under similar conditions as a reference.

Static ToF-SIMS analyses were carried out using an ION-TOF 'TOF-SIMS IV – 200' instrument (ION-TOF GmbH, Münster, Germany) of single-stage reflectron design.[32] Positive and negative ion spectra of the samples were obtained using a Bi^{32+} focused liquid metal ion gun at 20keV energy, incident at 45° to the surface normal and operated in 'bunched' mode for high mass resolution. This mode used 7ns duration ion pulses at 10kHz repetition rate. Charge compensation was effected by low-energy (ca. 20eV) electrons provided by a flood gun. The total ion dose density was less than 5×10^{16} ions m^{-2} in all cases. The topography of the sample surface and the ion gun mode of operation limited the mass resolution in this work to *ca.* $m/\Delta m$ = 4000.

Positive and negative ion static SIMS spectra of the samples were recorded in triplicate at room temperature with a 128 × 128 pixel raster and a field of view of 50µm × 50µm. Sample preparation and data analysis was carried out according to the procedure detailed in the SI.

Raman analysis

Raman analysis was performed using a Renishaw inVia Raman Microscope equipped with a laser operating at a wavelength of 785 nm. The analysis was undertaken by focusing the laser with a 50x long distance objective. Laser power at the sample surface was set to 66mW at the sample surface and the acquisition time was set between 3 and 10s for each of the 10 accumulations acquired. Each

spectrum was taken over the wavenumber range 77–1290cm^{-1}. Three spectra per sample were acquired to evaluate variations between different locations. Prior to the analysis, the spectrometer was calibrated using a monocrystalline silicon standard specimen. Renishaw WiRe 4.0 software was applied for peak fitting and deconvolution of Raman spectra. The sample was initially kept in a N_2-rich atmosphere inside the glass cell with quartz window to prevent contamination by atmospheric CO_2. To investigate the initial stage of carbonation, the quartz window was removed and spectral acquisition of the carbonate phases formed at 23°C and 30%±10%RH was started. These conditions reduced the carbonation rate and, therefore provided better evidence of the phase transformations related to carbonation. Spectra were taken at intervals up to 55 minutes from initial exposure of the sample to air.

SEM analysis

SEM images were obtained using a JEOL field emission scanning electron microscope (FESEM) model JSM6301F. Working distance for scanning and acquiring the images was 7mm, accelerating voltage was of 5kV and the spot size 7nm. Prior to analysis the sample powder was fixed to a metal holder using a double-sided carbon tape and then dried for 24 hours in a vacuum chamber before application of a 10nm thick layer of chromium using a Quantum Q 150T Turbo-Pumped Sputter Coater to prevent surface charging. Once removed from the sputter coater, the sample was immediately inserted into the SEM and analyzed.

Computational procedure

Simulations were used to determine the vibrational shifts and Raman spectra for ^{16}O and ^{18}O-calcium hydroxide ($Ca(^{16}OH)_2$, $Ca(^{18}OH)_2$ respectively), as well as calcite containing different amounts of ^{18}O ($CaC^{18}O_x{}^{16}O_{(3-x)}$ with x=0,1,2,3). Calculations were performed at the DFT level using the VASP[36-36] code with the PBE[39-40] exchange-correlation functionals including the van der Waals correction optB86b-vdW[41,42], which improves the description of layered materials. The Brillouin zone was sampled using 4 × 4 × 4 Monkhorst-Pack k-point mesh for portlandite and 4 × 4 × 1 for calcite with a

plane wave cut-off of 500 eV. Convergence criteria were 10^{-8} eV for the electronic relaxation and 10^{-4} eV $Å^{-1}$ for ionic forces, allowing both the atoms and lattice to relax.

The calculated structure of portlandite contains 1 $Ca(OH)_2$ unit and had lattice parameters of a = b = 3.573Å, c = 4.794Å, α = β = 90° and γ = 120°, which compared well with the experimental values of Desgranges *et al*.[44]. The calculated structure of calcite contained 6 $CaCO_3$ units and had lattice parameters of a = b = 5.03Å, c = 16.80Å, α = β = 90° and γ = 120°, and agreed with the experimental values of Effenberger et al.[45]

From the minimized structures, the vibrational frequencies were obtained using finite displacements[46] and the Raman activity[47,48] was then estimated by calculating the polarizability of the vibrational modes. As noted, the minimized structure for portlandite compares well with the experimental values (Table S1) and this model has recently been shown to perform well for the calcium oxide and carbonate.[49,50] Additional calculations were undertaken to predict the shift in Raman frequencies due to isotopic substitution and compared to the DFT predicted Raman active peaks. Each vibrational mode is composed of specific motions of the atomic species associated with it. The interaction between the species involved can be related to a bond and this can be illustrated by considering a diatomic molecule. From the initial calculation we obtain a force constant *k* from which the frequency, *f,* can be calculated according to Equation 1, where μ is the reduced mass of the components of the mode given by Equation 2, and, m_1 and m_2 are the masses vibrating.

$$f = \sqrt{\frac{k}{\mu}} \qquad (1)$$

$$\mu = \frac{m_1 m_2}{m_1 + m_2} \qquad (2)$$

When accounting for the difference in mass between ^{16}O and ^{18}O the reduced mass changes according to the O isotope. In practice, we evaluate and diagonalise the complete mass-weighted force constant matrix.[51-53]

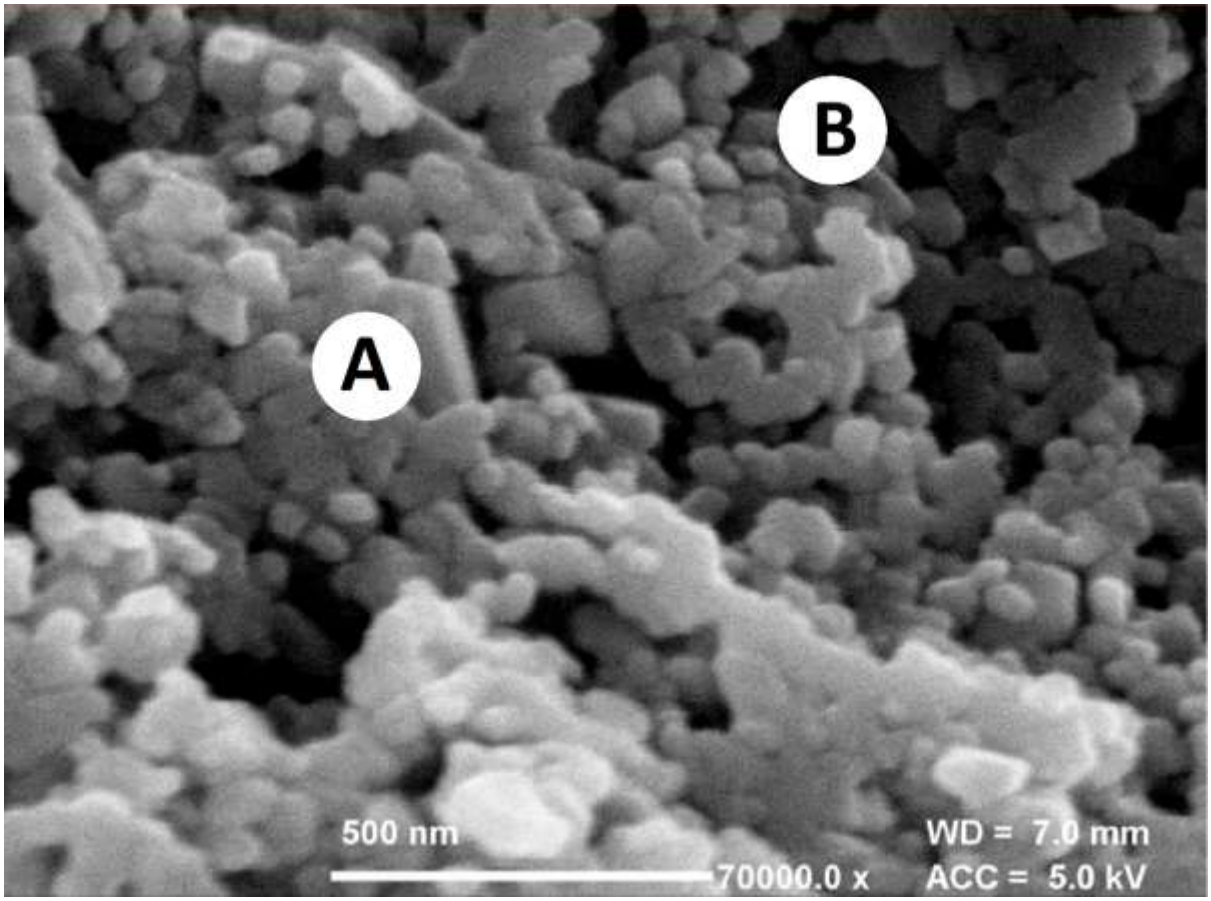

Figure 1 - FESEM image of the $Ca(^{18}OH)_2$ produced by reacting calcium with $H_2{}^{18}O$. Some hexagonal plate-shaped nano-particles typical of $Ca(OH)_2$ are visible (A) but the material is mostly in smaller irregular shaped crystalline particles (B).

Results

SEM and Raman results

A microscopic FESEM image is shown in Figure 1 of a $Ca(^{18}OH)_2$ sample comprising hexagonal plate-shaped crystals of 200-400nm and crystalline particles of 70-150 nm. The presence of many irregular shaped crystals is consistent with the exothermic reaction of calcium with water. The rapid evaporation of the excess $H_2{}^{18}O$ is likely to have resulted in a high nucleation rate. This then subsequently led to numerous seed crystals competing for ions from which to grow and provided a limited opportunity for Ostwald ripening of typical hexagonal nanoparticles, The reaction and storage conditions ensured that no carbonation could take place and only $Ca(OH)_2$ could form.

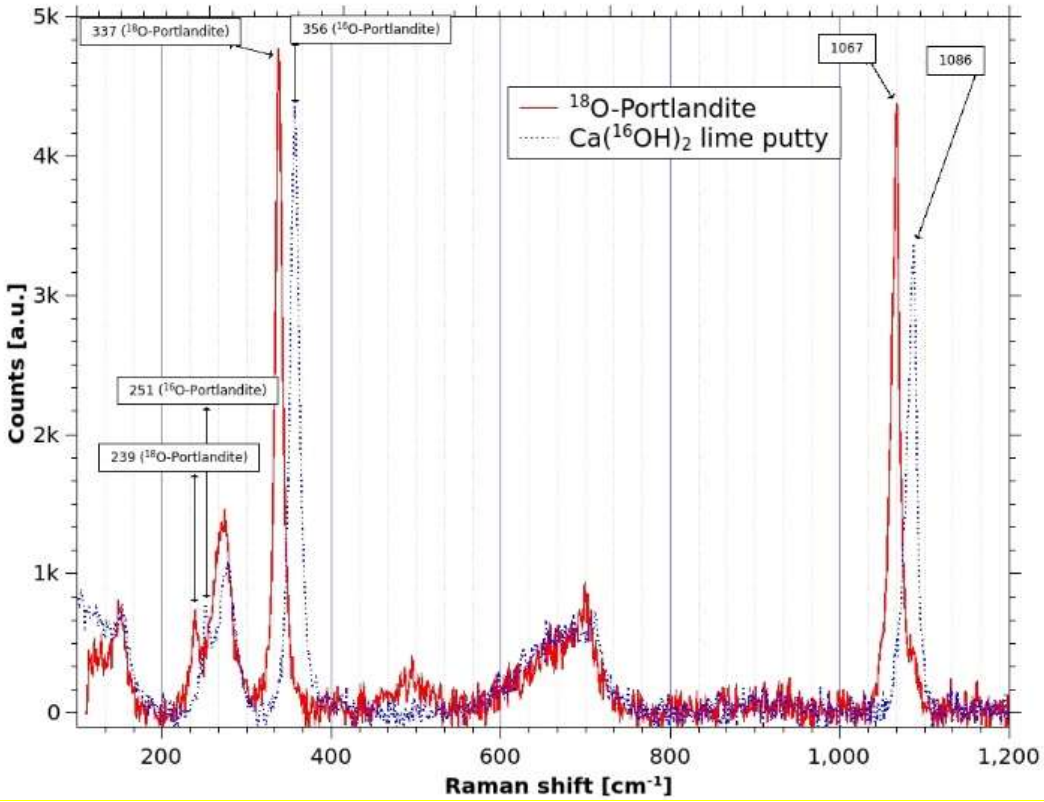

Figure 2 - Raman spectrum of the Ca(^{18}OH)$_2$ produced during the experiments, compared with the Raman spectrum of a generic ^{16}O-Ca(OH)$_2$ (lime putty).

Figure 2 shows the Raman spectrum from 100 to 1200 cm^{-1} of Ca(^{18}OH)$_2$ after about 10 minutes from exposure to air, compared with the spectrum of a generic ^{16}O-lime putty partially exposed to air. Both spectra contain portlandite and calcite peaks. Several peaks of Ca(^{18}OH)$_2$ are shifted to lower wavenumbers compared to the Ca(^{16}OH)$_2$. Of the peaks due to portlandite the peak at 356cm^{-1} is shifted ~-19cm^{-1} to 337cm^{-1}, the peak at 251cm^{-1} is shifted ~-12cm^{-1} to 239cm^{-1}. We also observe that the peak at 1086 cm^{-1} resulting from some carbonation of the samples is shifted ~-19cm^{-1} to 1067 cm^{-1}.

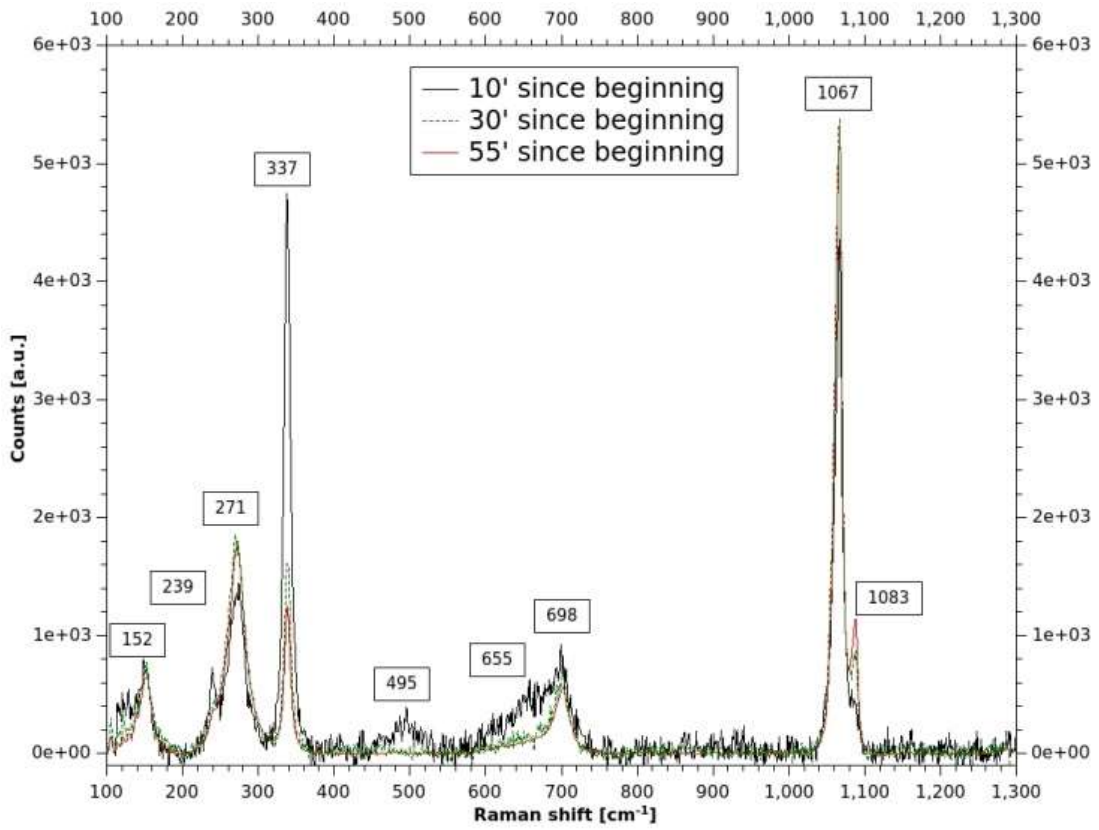

Figure 3 - Raman spectrum of the $Ca(^{18}OH)_2$ produced partially carbonated. Spectra taken after 10', 30' 55' since the beginning of the tests, which exposes the sample to air.

Figure 3 shows the Raman spectra from 100 to 1300 cm^{-1} of the $Ca(^{18}OH)_2$ produced, after 10, 30 and 55 minutes from opening of the cell, which allowed contact of the sample with air. Peaks at 239, 337 and 655 cm^{-1} are related to $Ca(^{18}OH)_2$ and become weaker over time. This provides evidence of $Ca(^{18}OH)_2$ reacting with atmospheric CO_2 containing ^{16}O and forming $CaCO_3$. According to our simulations, peaks at 152, 271, 698 and 1067 cm^{-1} can be best modelled as calcite with each carbonate containing a single ^{18}O (although it is possible that the peak at 1067cm^{-1} also includes a contribution of ^{18}O-enriched ACC; see discussion later in this paragraph). These peaks are shifted to lower wavenumbers compared to literature spectra of ^{16}O-calcite (Table S4). The intensity of the peak at 152 cm^{-1} remains unaltered over time, whereas the intensity of peaks at 271, 698 and 1083 cm^{-1} increase, suggesting progression of the carbonation reaction with the formation of an increasing amounts of ^{16}O-calcite. The broad peaks at 450 cm^{-1} disappearing after 10 minutes

reaction, suggests the presence of a metastable phase such as ACC (main peak included in the 1067cm^{-1} peak as previously mentioned).

Computation Results

Table 1 compares Raman active modes of a natural ($Ca(^{16}OH)_2$) and an isotopically labelled ($Ca(^{18}OH)_2$) portlandite calculated using DFT with experimental values. Although, the relative positions of the peaks are captured for both minerals, there is a systematic displacement of the predicted peaks relative to the experimental positions[53]. This is a well-known effect of DFT calculations and relates to the estimation of bond strengths.

Table 1 - Comparison of experimental and simulated Raman active modes of portlandite. The Raman shift due to the different O isotopes, denoted Δ, is compared to the theoretically derived values (Equation 1).

Experiment [cm^{-1}]			Simulation [cm^{-1}]			Theory [cm^{-1}]
$Ca(^{16}OH)_2$	$Ca(^{18}OH)_2$	Δ	$Ca(^{16}OH)_2$	$Ca(^{18}OH)_2$	Δ	Δ
251	239	-12	256	242	-14	-14
356	337	-19	381	361	-20	-19
675	675	0	715	715	0	0

The two low frequency peaks of portlandite are associated with vibrations of the hydroxide ions relative to each other in plane and out of plane. In the case where two hydroxide ions are vibrating as whole units the individual masses in the pure case are $m_1=m_2=17$ while for full isotopic substitution with ^{18}O these increase to $m_1=m_2=19$. The reduced masses are 17/2 and 19/2 respectively, and thus the theoretical treatment as in Equation 1 predicts the isotopically doped system has a frequency to $(17/19)^{1/2}$ of the natural case corresponding to shifts of -14cm^{-1} (for peak 1 at 251cm^{-1}) and -19cm^{-1} (peak 2). In contrast, the high frequency portlandite peak at 675cm^{-1} is

associated with the rocking mode of individual hydroxide ions. Since this is a rotational vibration, any shift is due not to the change in effective mass associated with isotopic substitution but with the moment of inertia. The resulting Raman shift due to isotopic composition is predicted to be ~0.3% (compared with ~5% in the previous cases) which is consistent with no observed shift in the experimental and simulated spectra. While Raman can be used to identify isotopic variation,[54] the comparison with calculation can help to identify the constitution of our samples and give insight into the processes during their formation.

Calcite with different isotopic composition ($CaC^{16}O_{3-x}{}^{18}O_x$) shows Raman shifts to lower wave number with increasing *x*, the number of ^{18}O per carbonate ion (Table 2). The peak at about 152 cm^{-1} in the experimental spectra is noisy and difficult to isolate in both the natural and ^{18}O-sample but the remaining Raman active peaks are relatively well defined and more easily characterized. Overall, the computational results are in good agreement with the measured spectra. The advantage of the calculation is that the vibrational motion associated with each active mode can be identified.[52] For example, we can clearly identify the peak at 1086cm^{-1} as the symmetric stretch of the C-O bond in the carbonate ions, whereas the peak at 700 cm^{-1} is an antisymmetric coupling between carbonate ions in different layers. The vibrations of the remaining peaks are complex motions of carbonate bending in different layers.

Table 2 - Comparison of experimental and simulated Raman active modes of calcite. In brackets the Raman shift due to the different O isotopes compared to $CaC^{16}O_3$. The two columns in the experimental results are related to carbonate phases with different ^{18}O content.

Peak	Experiment [cm^{-1}]		Simulation [cm^{-1}]			
	$CaCO_3$ $^{18}O > {}^{16}O$	$CaCO_3$ $^{18}O < {}^{16}O$	$CaC^{16}O_3$	$CaC^{18}O^{16}O_2$	$CaC^{18}O_2{}^{16}O$	$CaC^{18}O_3$
1	152	152	159-165	156-162 (-3)	154-160 (-5)	151-157 (-8)
2	277	282	293	288 (-5)	285 (-8)	282 (-11)

3	698	713	680	672-665 (-8/-15)	661-652 (-19/-28)	645 (-35)
4	1066	1086	1055	1036 (-19)	1015 (-40)	995 (-60)

ToF-SIMS Results

Tof-SIMS allows the determination of the elemental, isotopic, or molecular composition of surfaces to a maximum depth of 1-2 nm. It is a destructive technique that reveals, using a mass spectrometer, the mass:charge ratio of secondary ions ejected from the surface when a primary ion beam is fired against it. Therefore, during the analysis secondary ions may be positively and negatively charged depending on their composition and mass. Data analysis has therefore to take into account both polarities. Full details of mass:charge ratio of ejected secondary ions considered in this study are in Tables S2 and S3 where a detailed analysis of the results is also reported. To assess the accuracy of the ToF-SIMS measurement, we tested an Analar $CaCO_3$ reference sample, which gave an average ^{18}O:^{16}O ratio of 0.021 (Table 3) in agreement with the isotopic ratio between 0.019 and 0.021[57-59] of naturally occurring samples. Data for the carbonated $Ca(^{18}OH)_2$ samples, show a reduction in the relative intensities of species containing ^{18}O over time, and a simultaneous increase of the intensities of species containing ^{16}O (Figures S1-S3 in the SI). Simultaneously, species containing carbon such as $[HC^{18}O_3]^-$ and $[C^{18}O_3]^-$ (Figures S1-S3) show an increase. This is clear evidence of the carbonation of portlandite surfaces as secondary ions ejected from the surface destruction have greater carbon content.

Table 3 reports the ^{18}O:^{16}O ratio calculated for all the secondary ions produced by the destruction of the surface over the duration of the experiment. Data shows an initial isotope ratio of 0.62 for positive ions and a ratio of 0.51 for negative ions. The weighted average value of 0.54 suggests that, at very early stages of the carbonation reaction, for every atom of ^{18}O in carbonate ions, there would be two ^{16}O (theoretical ^{18}O:^{16}O ratio 0.5). However, from day 0 to day 1 the data shows a dramatic decrease in the ^{18}O:^{16}O ratio to a value of 0.038 that shows little variation in the following days. This value shows little variation after 137 days of carbonation. The isotope ratio for positive and negative

species converges towards the same value of 0.046, which is approximately double the value for natural samples.

Table 3 - ^{18}O:^{16}O ratio calculated from the intensity of the ToF-SIMS counts for the ionic species with positive and negative polarity

	Analar $CaCO_3$	Carbonated $Ca(^{18}OH)_2$			
		Day 0	Day 1	Day 8	Day 137
$[^{18}O/^{16}O]^+$	0.035	0.616	0.057	0.044	0.046
$[^{18}O/^{16}O]^-$	0.007	0.509	0.032	0.029	0.046
Weighted Average	0.014	0.537	0.038	0.033	0.046

Discussion

The combination of complementary results from the vibrational fingerprint of the materials with different isotopic composition and the ToF-SIMS experiments show that we can elucidate the carbonation mechanism of hydrous materials. However, before discussing our data, the role of the pH in the carbonate precipitation and on the behavior of different isotopes during the process should be highlighted.

Recent work on the precipitation of carbonates in natural systems (i.e. at approximately neutral pH) shows that an isotopic equilibrium is reached between the solution and the precipitated solid, which only depends on temperature. [34,59] On the other hand, precipitation of carbonates from saturated solutions of $Ca(OH)_2$ take place under high pH (12.4 at 23°C)[14] and therefore is in non-equilibrium conditions. As a consequence, the main phenomenon producing fractionation during precipitation is the reaction kinetics related to the solution high pH.[29-33] At pH values above 9, various authors[29,31-33] suggested that the direct reaction of CO_2 with the hydroxyl group (OH^-) produced by the dissociation of water is the primary pathway for carbonate ion formation (Equation 3). [29] This pathway is suggested to be faster than the one leading to the formation of CO_3^{2-} from the

reaction of CO_2 in natural waters at neutral pH[58] (Equations 4-7) and, consequently, it prevents isotope equilibration of gaseous $CO_{2(g)}$ with the dissolved $CO_{2(aq)}$ (Equation 4). Since heavier isotopes react slower than lighter isotopes, in the carbonate precipitates at high pH we would expect a lower concentration of ^{18}O and ^{13}C compared to the carbonates precipitated under equilibrium conditions.[29] Examples of carbonate phases with a very different isotope signature are limestone of marine and continental origins, and carbonates produced during cement setting.[31-33]

$$CO_{2(aq)} + OH^- \leftrightarrow CO_3^{2-} + H^+ \quad (3)$$

$$CO_{2(g)} \leftrightarrow CO_{2(aq)} \quad (4)$$

$$CO_{2(aq)} + H_2O_{(l)} \leftrightarrow H_2CO_{3(aq)} \quad (5)$$

$$H_2CO_{3(aq)} \leftrightarrow HCO_{3(aq)}^- + H_{(aq)}^+ \quad (6)$$

$$HCO_{3(aq)}^- \leftrightarrow CO_{3(aq)}^{2-} + H_{(aq)}^+ \quad (7)$$

Equilibrium in Equation 3 implies that the carbonate ion contains a mixture of the isotopic composition of aqueous $CO_{2(aq)}$ (similar to the isotopic composition of gaseous $CO_{2(g)}$) and OH^- ions.[29,31,33] The ^{18}O composition of these carbonates ($n^{18}O$) can be described by considering the abundance of ^{18}O in the different species, according to Equation 8.

$$n^{18}O_{carbonate} \leftrightarrow \frac{1}{3}n^{18}O_{OH} + \frac{2}{3}n^{18}O_{CO2(g)} \quad (8)$$

Letolle et al.[29] have calculated that one third of the oxygen in the carbonates formed under high pH conditions, is provided by the OH^- ions originated from the dissociation of H_2O molecules catalyzing the reaction between $Ca(OH)_2$ and aqueous $CO_{2(aq)}$. This implies that the ^{18}O content of OH^- groups is related to the isotopic composition of H_2O. Letolle et al.[29], however, did not provide any information on the role of OH^- ions produced by the dissolution of $Ca(OH)_2$ on the isotopic composition of carbonate phases.

To demonstrate that hydroxyl groups from the surface have a fundamental role in the formation of carbonate phases, we have studied $Ca(^{18}OH)_2$ samples containing ^{18}O. Therefore, during the carbonation of $Ca(^{18}OH)_2$, the sample itself is by far the most significant source of ^{18}O (a very limited contribution can be due to the CO_2 and H_2O [60,61]) whereas the atmospheric water and CO_2 are the only source of ^{16}O. Any mixture of the isotope in the resulting carbonate phases provides the most likely source of oxygen in the formation of carbonate ions and therefore the carbonation mechanism.

The Raman spectrum of $Ca(^{18}OH)_2$ confirms the purity of the sample but also the high surface reactivity, as demonstrated by the formation of carbonate phases after 10 minutes from exposure to atmospheric CO_2. This is in agreement with the results of previous studies on the carbonation kinetics and on the role of water vapor on the $Ca(OH)_2/CO_2$ solid-gas reaction.[12,62] The shift observed for the Raman peaks of portlandite and calcite can be associated with variations in the isotopic composition of the minerals and are supported by ab initio calculations. In the case of portlandite, the shifts in the Raman peaks arise from substitution of all the ^{16}O with ^{18}O (Figure 2), whereas the shift in the Raman peaks of carbonate phases formed after the reaction with atmospheric CO_2 arise from partial substitution of ^{16}O with ^{18}O (Figure 3). DFT data (Table 2) support that the experimental peaks at 152, 271, 698 and 1066 cm^{-1} are associated with calcite containing 1/3 of ^{18}O (^{18}O:^{16}O ratio 0.5). The main vibrational fingerprint of this phase could be identified in the peak at 1066 cm^{-1} (Figure 3). The peak at 1083 cm^{-1} belongs to ^{16}O-calcite, which is a minor phase at the beginning of the reaction which then grows over the time.

SIMS results allow calculation of the ^{18}O:^{16}O ratio for the secondary ions ejected from surface destruction. At the early stage of carbonation (~3 minutes exposure to air), the ratio is of 0.51 (Table 3). This value is in good agreement with the results of our theoretical analysis of Raman shifts and with Letolle's proposition[29]. This indicated that in carbonate precipitates at high pH, 2/3 of oxygen is supplied by CO_2 whereas 1/3 of the oxygen is provided by OH^- ions. However, unlike Latolle's proposition suggesting that the OH^- groups involved in the carbonation originate from the

dissociation of H_2O molecules, our results clearly demonstrate that the $Ca(OH)_2$ plays an important role in the formation of hydroxyl groups. ToF-SIMS data displays carbonate species that contain 1/3 of ^{18}O (the remaining 2/3 comes from $C^{16}O_2$), which in our case can only be produced by the dissolution of the surface and not by the dissociation of adsorbed water molecules, which comprise mainly ^{16}O. This is also supported by PHREEQC[57,63] modelling (see model description and Table S5 in the SI) showing that the concentration of OH^- ions produced by the dissolution of $Ca(OH)_2$ in pure water at 25°C, is several orders magnitude greater than the concentration of OH^- ions produced by the natural dissociation of pure water. Therefore, the OH^- ions from $Ca(OH)_2$ are more likely to take part in the carbonation reaction compared to those from water. As a consequence, it is possible to infer that in highly alkaline conditions, the isotopic composition of precipitated carbonates, which is generally described by Equation 8, can be rewritten by considering the abundance of ^{18}O in the CO_2 and in the $Ca(OH)_2$ as reported in Equation 9. This new equation marks the very early stage of the carbonation reaction where the dissolution of the surface is the rate-limiting step. Although this equation is a simplification of the real process, since it omits contributions from the equilibration of $^{18}OH^-$ from the surface and from water, it can be used to describe the process in basic terms.

$$n^{18}O_{carbonate} \leftrightarrow \frac{1}{2} n^{18}O_{Ca(OH)_2} + \frac{2}{2} n^{18}O_{CO2(g)} \qquad (9)$$

Subsequent to the formation of ^{18}O rich carbonate phases in the first stage of the carbonation mechanisms, when the dissolution of portlandite surfaces must occur, our ToF-SIMS data show a dramatic reduction in ^{18}O:^{16}O ratio within the first day of carbonation (Table S6). This is also shown by the growth of the Raman peak at 1083 cm^{-1} of ^{16}O-calcite over time (Figure 3) and can be explained by the transformation of the initial metastable carbonates into more stable phases over time.[64-77] Figure 3 shows the disappearance over time of a peak at 495cm^{-1} that can be related to metastable hydrated phases[55]. A possible explanation of this re-equilibration of ^{18}O:^{16}O ratio is the dissolution of metastable phases that give up some ^{18}O and the subsequent recrystallization of more

stable phases that acquire ^{16}O during the precipitation process occurring under equilibrium conditions.

This marks the second stage of carbonation, which involves the transformation carbonate phases from lesser stable to more stable forms. A detailed explanation of this transformation has been recently provided by Rodriguez Navarro et al.[27]

Earlier, Rodriguez-Blanco et al.[70] described the transformation mechanism of ACC to calcite as a two stage process: 1) ACC particles rapidly dehydrate and crystallize forming individual particles of vaterite; 2) the vaterite dissolves and re-precipitates as calcite (Ogino et al.[71] also confirmed the latter stage also for aragonite). Stage 1, mainly entails the release of water molecules initially embedded in the structure of hydrated phases. Stage 2, involves the release of CO_3^{2-} ions that, according to equations 2-5, can lead to an exchange of oxygen atoms with the water molecules. We infer that our data is consistent with this proposition. The oxygen exchange and the formation of new carbonate phases richer in ^{16}O at the top of the carbonate phases initially formed (stage 1) explains the sudden variation of the ^{18}O:^{16}O ratio within the first 24h. Therefore, it is possible to infer that, whereas precipitation of meta-stable phases takes place under non-equilibrium conditions (i.e. at high pH, which does not allow isotope equilibration), the dissolution-and-precipitation mechanism leading to the formation of stable carbonate phases and the precipitation of new carbonate phases richer in ^{16}O, occurs at lower pH allowing an isotopic equilibrium of carbonates. It is worth noting that in our experiments this equilibration occurred within the initial 24 hours even at 50% RH (a relatively low RH value for carbonation) and this suggests that stage 2 of the carbonation is a fast kinetic pathway.

Conclusions

Our results show new insights in the carbonation mechanism of portlandite. They demonstrate that during the early stage of the carbonation reaction (first 3 minutes, in our experiments) the surface hydroxyl groups are the source of oxygen for the formation of carbonate ions and hence the growth of carbonate begins by the dissolution of hydroxyl and calcium ions followed by the

formation of metastable calcium carbonate. The second stage of the reaction occurs within the 24h after the carbonation started. This involves the transformation of the metastable carbonate phases into stable calcite. During this transformation there is a release of water, which is the source of oxygen for the formation of new carbonate ions.

Our results show how artificial isotopic doping can be used to study processes such as carbonation and have brought new insights into the early carbonation process. This knowledge should further the understanding of many processes involving carbonation such as carbon sequestration technologies, carbonation of construction materials, precipitated carbonate products and geological disposal facilities for nuclear waste.

Acknowledgements

The authors would like to thank the Engineering and Physical Sciences Research Council (EPSRC) for financial support through project EP/K025597/1. The computational work has made use of ARCHER, the UK's national HPC, via the Materials Chemistry Consortium funded by the EPSRC (EP/L000202) in addition to the University of Bath's HPC resource. The authors are grateful to Mrs Ursula Potter and Dr Philip Fletcher of the Microscope and Analysis Suite of the University of Bath for assistance with SEM imaging and Raman spectroscopy. All data supporting this study are openly available from the University of Bath data archive at 10.15125/BATH-00240.

Supporting Information Description

(1) ToF-SIMS sample preparation; (2) ToF-SIMS data analysis; (3) PHREEQC calculations; (4) detailed plots of the SIMS results; (4) experimental and simulated lattice parameters for portlandite; (5) Plot of the ^{18}O:^{16}O ratio over the time; (6) Table of experimental and simulated lattice parameters for portlandite; (7) List of all ions considered in this research; (8) list of ions considered for calculating the ^{18}O:^{16}O ratio; (9) peak position of the Rama spectra for different $CaCO_3$ phases; (10)

OH^- concentration in different aqueous solutions, calculated using PHREEQC. This information is available free of charge via the Internet at http://pubs.acs.org.

References

1) Blamey, J.; Lu, D. Y.; Fennell, P. S.; Anthony, E. J. Reactivation of CaO-based sorbents for CO_2 capture: mechanism for the carbonation of $Ca(OH)_2$, Industrial & Engineering Chemistry Research. **2011**, 50 (17), 10329-10334.

2) Zhao, L.; Sang, L.; Chen, J.; Ji, J.; Teng, H. H. Aqueous carbonation of natural brucite: relevance to CO_2 sequestration, *Environmental Science & Technology* **2010**, 44 (1), 406-411

3) Sawell, S.E.; Chandler, A.J.; Eighmy, T.T.; Hartlan, J.; Hjelmar, O.; Kosson, D.; van der Sloot, H.A.; Vehlow, J. The international ash working group: A treatise on residues from {MSW} incinerators, In Environmental Aspects of Construction with Waste Materials; van der Sloot, H.A.; Goumans, J.J.J.M.; Aalbers, Th.G. Eds. Proceeding of the International Conference on Environmental Implications of Construction Materials and Technology Developments volume 60 of Studies in Environmental Science; Elsevier: **1994**; pp 3-6.

4) Gartner, E.; Hirao, H. A review of alternative approaches to the reduction of CO_2 emissions associated with the manufacture of the binder phase in concrete. *Cement and Concrete Research*. **2015**, 78 Part A, 126-142.

5) Pesce, G.L.; Bowen, C. R.; Rocha, J.; Sardo, M.; Allen, G.; Walker, P.; Denuault, G.; Serrapede, M.; Ball, R. J. Monitoring hydration in lime-metakaolin composites using electrochemical impedance spectroscopy and nuclear magnetic resonance spectroscopy. *Clay Minerals.* **2014**, 49, 341-358.

6) Berger, R. Calcium Hydroxide: Its Role in the Fracture of Tricalcium Silicate Paste. *Science*, **1972**, 175(4022), 626-629

7) Corkhill, C.L.; Bridge, J.W.; Chen, X.C. et al. Real-Time Gamma Imaging of Technetium Transport through Natural and Engineered Porous Materials for Radioactive Waste Disposal. *Environmental Science & Technology*. **2013**, 47(23), 13857-13864

8) Ewing, R.C. Long-term storage of spent nuclear fuel. *Nature Materials*. **2015**, 14(4), 252-257

9) Hovelmann, J.; Putnis, C. V.; Ruiz-Agudo, E.; Austrheim, H. Direct nanoscale observations of CO_2 sequestration during brucite [$Mg(OH)_2$] dissolution, *Environmental Science & Technology*. **2012**, 46(9), 5253-5260.

10) Allen, A.J.; Jeffrey, J.; Jennings, H.M. Composition and density of nanoscale calcium silicate-hydrate in cement. *Nature Materials*. **2007**, 6(4), 311-316

11) Ruiz-Agudo, E.; Kudlacz, K.; Putnis, C. V.; Putnis, A.; Rodriguez-Navarro, C. Dissolution and carbonation of portlandite [$Ca(OH)_2$] single crystals, *Environmental Science & Technology*. **2013**, 47(19), 11342-11349.

12) Cizer, O.; Rodriguez-Navarro, C.; Ruiz-Agudo, E.; Elsen, J.; Gemert, D.; Balen, K. Phase and morphology evolution of calcium carbonate precipitated by carbonation of hydrated lime, *Journal of Materials Science*. **2012**, 47 (16), 6151-6165.

13) Cizer, O.; Van Balen, K.; Elsen, J.; Van Gemert, D. Realtime investigation of reaction rate and mineral phase modifications of lime carbonation. *Construction and Building Materials*. **2012**, 35, 741-751

14) Serrapede, M.; Pesce, G.L.; Ball, R.J.; Denuault, G. Nanostructured Pd hydride microelectrodes: In situ monitoring of pH variations in a porous medium. *Analytical Chemistry*. **2014**, 86 (12), 5758-5765

15) Kitamura, M.; Konno, H.; Yasui, A.; Masuoka H. Controlling factors and mechanism of reactive crystallization of calcium carbonate polymorphs from calcium hydroxide suspensions. *Journal of Crystal Growth*. **2002**, 236 (1-3), 323–332.

16) Domingo, C.; Garcia-Carmona, J.; Loste, E.; Fanovich, A.; Fraile, J.; Gomez-Morales, J. Control of calcium carbonate morphology by precipitation in compressed and supercritical carbon dioxide media. *Journal of Crystal Growth*. **2004**, 271 (1-2), 268–273.

17) Sheng Han, Y.; Hadiko, G.; Fuji, M.; Takahashi, M. Crystallization and transformation of vaterite at controlled pH. *Journal of Crystal Growth*. **2006**, 289 (1), 269–274.

18) Euvrard, M.; Membrey, F.; Filiatre, C.; Foissy, A.. Crystallization of calcium carbonate at a solid/liquid interface examined by reflection of a laser beam. *Journal of Crystal Growth*. **2004**, 265 (1-2), 322–330.

19) Despotou, E.; Schlegel, T.; Shtiza, A.; Verhelst, F. Literature study on the rate and mechanism of carbonation of lime in mortars, In *Proceeding of the 9th International Masonry Conference*. **2014**. Guimaraes, Portugal on 7-9 July 2014.

20) Moorehead, D.R. Cementation by the carbonation of hydrated lime. *Cement and Concrete Research*. **1986**, 16 (5), 700-708.

21) Stepkowska, E.T. Hypothetical transformation of $Ca(OH)_2$ into $CaCO_3$ in solid-state reactions of portland cement. *Journal of Thermal Analysis and Calorimetry*. **2005**, 80 (3), 727-733.

22) Montes-Hernandez, G.; Daval, D.; Chiriac, R.; Renard, F. Growth of nanosized calcite through gas-solid carbonation of nanosized portlandite under anisobaric conditions. *Crystal Growth & Design*. **2010**, 10 (11), 4823-4830.

23) Yang, T.; Keller, B.; Magyari, E.; Hametner, K.; Gunther, D. Direct observation of the carbonation process on the surface of calcium hydroxide crystals in hardened cement

paste using an atomic force microscope, *Journal of Materials Science*. **2003**, 38 (9), 1909-1916.

24) Johnstone J. R.; Glasser, F. P. Carbonation of portlandite single crystals and portlandite in cement paste, In 9th International Congress on the Chemistry of Cement volume 5 , **1992**, 370-376.

25) Rodriguez Navarro C.; Vettori I.; Ruiz-Agudo E. Kinetics and Mechanism of Calcium Hydroxide Conversion into Calcium Alkoxides: Implications in Heritage Conservation Using Nanolimes, *Langmuir*, **2016**, 32(20), 5183-5194

26) Rodriguez-Navarro C.; Elerta K.; Ševčíkb R. Amorphous and crystalline calcium carbonate phases during carbonation of nanolimes: implications in heritage conservation, CrystEngComm. **2016**, 18, 6594-6607

27) Rodriguez-Navarro, C.; Kudłacz, K.; Cizer, Ö.; Ruiz-Agudo, E. Formation of amorphous calcium carbonate and its transformation into mesostructured calcite. CrystEngComm, 2015, 17(1), 58-72

28) Galan, I.; Glasser, F.P.; Baza, D.; Andrade, C., Assessment of the protective effect of carbonation on portlandite crystals. *Cement and Concrete Research*, **2015**, 74, 68-77

29) Letolle, R.; Gegout, P.; Gaveau, B.; Moranville-Regourd, M. Fractionnement isotopique de l'oxygène-18 dans la précipitation des carbonates a pH très élevé. *Comptes Rendus de l'Académie des Sciences.* **1990**, 310, 547-552.

30) Van Strydonck, M.; Dupas, M.; Keppens, E. "Isotopic fractionation of oxygen and carbon in lime mortar under natural environment conditions. *Radiocarbon*. **1989**, 31, 610-618.

31) Létolle, R.; Gégout, P.; Moranville-Regourd, M.; Gaveau, B. Carbon-13 and oxygen-18 mass spectrometry as a potential tool for the study of carbonate phases in concrete. *Journal of the American Ceramic Society*. **1990**, 73, 3617-3625.

32) Rafai, N.; Letolle, R.; Blanc, P.; Person, A.; Gegout, P. Isotope geochemistry (13C, 18O) of carbonation processes in concretes. *Cement and Concrete Research*. **1991**, 21, 368-377.

33) Letolle, R.; Gegout, P.; Rafai, N.; Revertegat, E. Stable isotopes of carbon and oxygen for the study of carbonation/decarbonation processes in concretes. *Cement and Concrete Research*. **1992**, 22, 235-240, Special Double Issue Proceedings of Symposium D of the E-MRS Fall Meeting 1991.

34) Kosednar-Legenstein, B.; Dietzel, M.; Leis, A.; Stingl, K. Stable carbon and oxygen isotope investigation in historical lime mortar and plaster. Results from field and experimental study. *Applied Geochemistry*. **2008**, 23, 2425-2437.

35) Schwieters J.; Cramer H.G.; Heller T.; Jürgens U.; Niehuis E.; Zehnpfenning J.; Benninghoven A. High mass resolution surface imaging with a time-of-flight secondary ion mass spectroscopy scanning microprobe J. *Vac. Sci. Technol. A*. **1991**; 9, 2864.

36) Kresse, G.; Furthmüller, J., Efficient iterative schemes for ab initio total-energy calculations using a plane-wave basis set. *Physical Review B*, **1996**, 54(16), 11169-11186

37) Kresse, G.; Hafner, J., Ab initio molecular-dynamics simulation of the liquid-metal\char21amorphous-semiconductor transition in germanium. *Physical Review B*, **1994**, 49(20), 14251-14269

38) Kresse, G.; Hafner, J., Ab initio molecular dynamics for liquid metals. *Physical Review B*, **1993**, 47(1), 558-561

39) Kresse, G.; Joubert, D., From ultrasoft pseudopotentials to the projector augmented-wave method. *Physical Review B*, **1999**, 59(3), 1758-1775

40) Perdew, J. P.; Burke, K.; Ernzerhof, M., Generalized Gradient Approximation Made Simple. *Physical Review Letters*, **1996**, 77 (18), 3865-3868

41) Klimeš, J.; Bowler, D. R.; Michaelides, A., Van der Waals density functionals applied to solids. *Physical Review B*, **2011**, 83(19), 195131

42) Klimeš, J.; Bowler, D. R.; Michaelides, A., Chemical accuracy for the van der Waals density functional. *Journal of Physics: Condensed Matter*. **2010**, 22(2), 022201

43) Wu, X.; Vanderbilt, D.; Hamann, D. R., Systematic treatment of displacements, strains, and electric fields in density-functional perturbation theory. *Physical Review B.* **2005**, 72(3), 035105

44) Desgranges, L.; Grebille, D.; Calvarin, G.; Chevrier, G.; Floquet, N.; Niepce, J.C. Hydrogen thermal motion in calcium hydroxide: $Ca(OH)_2$, *Acta Crystallographica, Section B: Structural Science*. **1993**. 49, 812-817

45) Effenberger, K. H. M.; Zemann, J. Crystal structure refinements of Magnesite, Calcite, Rhodochrosite, Siderite, Smithonite, and Dolomite, with the discussion of some aspects of the stereochemistry of Calcite type carbonates, *Zeitschrift fuer Kristallographie.* **1981**, 156, 223-243

46) Fonari, A.; Stauffer, S., vasp_raman.py. https://github.com/raman-sc/VASP/: **2013**

47) Porezag, D.; Pederson, M. R., Infrared intensities and Raman-scattering activities within density-functional theory. *Physical Review B.* **1996**, 54 (11), 7830-7836

48) Porezag, D.; Pederson, M. R. Infrared intensities and Raman-scattering activities within density-functional theory. *Physical Review B.* **1996**, 54, 7830-7836

49) Andreassen, J.-P. Formation mechanism and morphology in precipitation of vaterite–nano-aggregation or crystal growth? *Journal of Crystal Growth*, **2005**, 274 (1-2), 256–264.

50) Grant, J.; Pesce, G.L.; Ball, R.J.; Molinari, M.; Parker, S.C. An Analytical and Computational Study to Resolve the Composition of Dolimitic Lime. *RCS Advances*, **2016**. 6(19), 16066-16072

51) Price, G.D.; Parker, S.C.; Leslie, M. The lattice-dynamics and thermodynamics of the Mg2SiO4 polymorphs. *Physics and Chemistry of Minerals*. **1987**, 15(2), 181-190

52) Cooke, D.J.; Parker, S.C.; Osguthorpe, D.J. Calculating the vibrational thermodynamic properties of bulk oxides using lattice dynamics and molecular dynamics. *Physical Review B*. **2003**, 67(13), 134306

53) Skelton, J.M.; Parker, S.C.; Togo, A.; Tanaka, I.; Walsh, A. Thermal physics of the lead chalcogenides PbS, PbSe, and PbTe from first principles. *Physical Review B*. **2014**, 89(20), 205203

54) Ruiz-Agudo E.; King H.E.; Patiño-López L.D.; Putnis C.V.; Geisler T.; Rodriguez-Navarro C.; Putnis A. Control of silicate weathering by interface-coupled dissolution-precipitation processes at the mineral-solution interface. *Geology*, 2016, 44(7), 567-570

55) Tlili, M. M.; Ben Amor, M.; Gabrielli, C.; Joiret, S.; Maurin, G.; & Rousseau, P. Characterization of $CaCO_3$ hydrates by micro-Raman spectroscopy. *J. Raman Spectrosc*. **2001,** 33, 10–16

56) De La Pierre, M.; Carteret, C; Maschio, L.; André, E; Orlando, R.; Dovesi, R., The Raman spectrum of $CaCO_3$ polymorphs calcite and aragonite: A combined experimental and computational study. **2014**. *The Journal of Chemical Physics*, 140, 164509

57) Appelo, C. A. J.; D., P. *Geochemistry, groundwater and pollution*; Taylor & Francis, **2005**.

58) Morse, J.; Mackenzie, F. *Geochemestry of sedimentary carbonate*; Developments in Sedimentology 48; Elsevier Science Publisher B.V., **1990**

59) Hoefs, J. *Stable Isotope Geochemistry*; Springer, **2004**

60) Trolier M.; White J.W.C.; Tans P.P.; Masarie K.A.; Gemery P.A. Monitoring the isotopic composition of atmospheric CO_2: Measurements from the NOAA Global Air Sampling Network. *Journal of Geophysical Research: Atmospheres*. 1996, 101(D20), 25897-25916

61) Lee X.; Sargent S.; Smith R.; Tanner B. In situ measurement of the water vapor 18O/16O isotope ratio for atmospheric and ecological applications. *Journal of Atmospheric and Oceanic Technology*. 2005, 22(5), 555-565)

62) Beruto, D.T.; Botter, R. Liquid-like H2O adsorption layers to catalyze the Ca(OH)2/CO2 solid–gas reaction and to form a non-protective solid product layer at 20°C. *Journal of the European Ceramic Society*, **2000**. 20(4), 497-503

63) Parkhurst, D. L.; Appelo, C. A. J. Description of Input and Examples for PHREEQC version 3: A Computer Program for Speciation, Batch-Reaction, One-Dimensional Transport, And Inverse Geochemical Calculations; U.S. Geological Survey: Reston, VA, **2013**.

64) Demichelis, R.; Raiteri, P.; Gale, J.D.; Quigley, D.; Gebauer, D. Stable prenucleation mineral clusters are liquid-like ionic polymers. *Nature Communications*. **2011**, 2, 590

65) Burns, K.; Wu, T.T.; Grant, C.S. Mechanisms of Calcite Dissolution Using Environmentally Benign Polyaspartic Acid: A Rotating Disk Study. *Langmuir*. **2003**, 19(14), 5669-5679

66) De Leeuw, N.H.; Parker, S.C. Surface Structure and Morphology of Calcium Carbonate Polymorphs Calcite, Aragonite, and Vaterite: An Atomistic Approach. *The Journal of Physical Chemistry B*. **1998,** 102(16), 2914-2922

67) Kerisit S.; Parker, S.C. Free Energy of Adsorption of Water and Metal Ions on the {10$\bar{1}$4} Calcite Surface. *Journal of the American Chemical Society*. **2004**, 126(32), 10152-10161

68) Perdikouri, C.; Putnis, C.V.; Kasioptas, A.; Putnis, A. An Atomic Force Microscopy Study of the Growth of Calcite Surface as a Function of Calcium/Total Carbonate Concentration Ratio in Solution at Constant Supersaturation. *Crystal Growth & Design*. **2009**, 9(10), 4344-4350

69) Kurganskaya, I.; Luttge, A. Kinetic Monte Carlo Approach To Study Carbonate Dissolution. *The Journal of Physical Chemistry C*. **2016,** 120, 6482-6492

70) Rodriguez-Blanco, J. D.; Shaw, S.; Benning, L. G. The kinetics and mechanisms of amorphous calcium carbonate (ACC) crystallization to calcite, via vaterite. *Nanoscale*. **2011**, 3, 265–271.

71) Ogino, T.; Suzuki, T.; Sawada, K. The rate and mechanism of polymorphic transformation of calcium carbonate in water. *Journal of Crystal Growth*. **1990**, 100 (1-2), 159–167.

72) Clarkson, J. R.; Price, T. J.; Adams, C. J. Role of metastable phases in the spontaneous precipitation of calcium carbonate. *J. Chem. Soc., Faraday Trans*. **1992**, 88, 243–249.

73) Kawano, J.; Shimobayashi, N.; Kitamura, M.; Shinoda, K.; Aikawa, N. Formation process of calcium carbonate from highly supersaturated solution. *Journal of Crystal Growth*. **2002**, 237-239, Part 1 (0), 419–423.

74) Carmona, J. G.; Morales, J. G.; Sainz, J. F.; Loste, E.; Clemente, R.R. The mechanism of precipitation of chain-like calcite. *Journal of Crystal Growth*, **2004**, 262 (1-4), 479–489.

75) Nehrke, G.; Van Cappellen, P. Framboidal vaterite aggregates and their transformation into calcite: a morphological study. *Journal of Crystal Growth*, **2006**, 287 (2), 528–530.

76) Nebel, H.; Neumann, M.; Mayer, C.; Epple, M. On the structure of amorphous calcium carbonates. a detailed study by solid-state NMR spectroscopy. *Inorganic Chemistry*, **2008**, 47 (17), 7874–7879.

77) Brecevic, L.; Kralj, D. On calcium carbonates: from fundamental research to application. *Croatica Chemica Acta*. **2007**, 80 (3-4), 467–484.

For Table of Contents Use Only

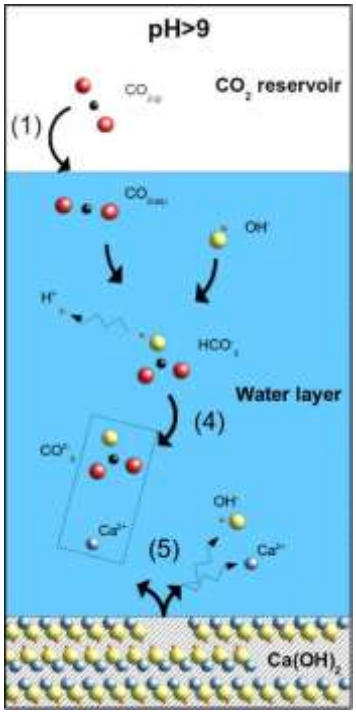

SYNOPSIS: At pH above 9, the direct reaction of CO_2 with the hydroxyl group produced by the dissolution of $Ca(OH)_2$ is the primary pathway for carbonate ion formation. This pathway is faster than the one leading to the formation of CO_3^{-2} from the dissolution of CO_2 in natural waters at neutral pH